



The effect of rotation on radial horizontal convection and Nusselt number scaling in a cylindrical container



Wisam K. Hussam, Tze K. Tsai, Gregory J. Sheard*

Department of Mechanical and Aerospace Engineering, Monash University, VIC 3800, Australia

ARTICLE INFO

Article history:

Received 21 December 2013

Received in revised form 1 May 2014

Accepted 4 May 2014

Keywords:

Heat transfer

Horizontal convection

Rotating flow

Nusselt number

Boundary-layer scaling

ABSTRACT

The effect of rotation on horizontal convection flow in a free-surface cylindrical enclosure driven by a radially increasing temperature profile along the base is investigated numerically and theoretically. The governing equations of mass, momentum and energy subject to Boussinesq approximation applied to gravity term, have been discretised using a spectral-element method for velocity and temperature fields. Results of a scaling analysis are compared with numerical simulations at a fixed Prandtl number $Pr = 6.14$, Reynolds numbers up to 3200, and Rayleigh number up to 3.2×10^{11} in an enclosure with height-to-radius ratio $H/R = 0.4$. The results show that heat transfer in rotating horizontal convection is significantly affected by rotation, and where rotation effects are significant, Nusselt number scalings adapted from Park and Whitehead and Stern describe the behaviour at moderate and high rotation rates, respectively. A scaling analysis is conducted to describe the suppression of convective flow at high rotation rates. Flows are characterised in terms of a rotation parameter and are divided into three regimes: a diffusive regime with Nusselt number independent of thermal forcing and rotation, a rotation-affected convective regime, and a convective regime unaffected by rotation at sufficiently high Rayleigh number.

© 2014 Elsevier Ltd. All rights reserved.

1. Introduction

Horizontal convection defines flows that are driven by temperature differentials imposed along a horizontal boundary [3]. This is in contrast to Rayleigh–Bénard convection in which the temperature differential is in the vertical direction [4,5]. Uneven heating applied across a horizontal boundary occurs in myriad geophysical and industrial systems, motivating further study into horizontal convection. In addition, the effect of rotation on convection flows is important in many industrial applications as well as in astrophysical and geophysical flows, including meridional overturning circulation in the ocean [6], Earth's core [7], as well as solar and mantle convection [8,9]. The combination of a radially forced horizontal convection and rotation in a cylindrical system idealises features of geophysical flows such as polar vortices in which solar heating of the surface has a latitudinal dependence, and this forms the basis of the system considered in the present study.

Laboratory fluid models for the study of polar vortices (e.g. [10,11]) have tended to feature mechanical forcing mechanisms

such as differentially rotating disks that are dissimilar to the geophysical processes, though these models have typically featured mechanical forcing mechanisms dissimilar to atmospheric mechanisms. In the present paper, the flow in a rotating cylindrical container driven by horizontal convection with radial forcing is considered. Cylinder rotation mimics Earth's rotation, and radial horizontal convection drives an annular fluid flux circulating outward radially near the base and returning poleward at the top surface. Conservation of angular momentum accelerates the angular velocity of poleward-moving fluid, spinning it into a vortex in an analogous manner to the generation of atmospheric polar vortices in the polar convection cell.

As a first approximation of the atmospheric system, this model disregards beta-plane effects associated with the change in the Coriolis effect with latitude in the vicinity of the pole [10]. Moreover, while the controlling parameters for this system are Reynolds and Rayleigh number, the parameters of interest when considering swirling atmospheric flows are typically the Rossby number (relating inertial to Coriolis forces) and the Ekman number (relating viscous to Coriolis forces). The Ekman number is related to the reciprocal of the Reynolds number, but the Rossby number, which relates the angular velocity of the model polar vortex to the background rotation, is flow-dependent.

* Corresponding author. Address: Department of Mechanical and Aerospace Engineering, Monash University, Room 350, building 82, VIC 3800, Australia. Tel.: +61 3 9905 1182.

E-mail address: Greg.Sheard@monash.edu (G.J. Sheard).

methodology is presented in Section 4, which describes the numerical method and model set up. Results and discussion follow in Section 5, with conclusions drawn in Section 6.

2. Mathematical formulation

The system under consideration consists of a free surface cylindrical enclosure rotating with an angular velocity Ω . It is filled with fluid, and a radially increasing temperature profile is imposed on the base. The tank radius R and height H combine to define an aspect ratio which in this study is fixed at $H/R = 0.4$. The system is depicted in Fig. 1.

The azimuthal velocity imposed on the impermeable base and side wall is $u_\theta = r\Omega$, where r is the radial coordinate. To model a free surface, a stress-free condition is imposed on the top boundary ($u_z = \partial u_r / \partial z = \partial u_\theta / \partial z = 0$). The side wall is thermally insulated by imposition of a zero normal temperature gradient, and to simplify the computational model, no heat loss is permitted through the stress-free top surface, which is also approximated as being thermally insulated. The linear temperature profile increases by δT from $r = 0$ to $r = R$ along the base to drive horizontal convection in the z - r plane.

A Boussinesq approximation for fluid buoyancy is employed, in which density differences in the fluid are neglected except through the gravity term in the momentum equation. Under this approximation the energy equation reduces to a scalar advection–diffusion equation for temperature which is evolved in conjunction with the velocity field. The fluid temperature is related linearly to the density via a thermal expansion coefficient α .

The dimensionless Navier–Stokes and energy equations governing a Boussinesq fluid may be written as

$$\hat{\nabla} \cdot \hat{\mathbf{u}} = 0, \quad (1)$$

$$\frac{\partial \hat{\mathbf{u}}}{\partial \hat{t}} = -(\hat{\mathbf{u}} \cdot \hat{\nabla}) \hat{\mathbf{u}} - \nabla \hat{p} + \frac{1}{Re} \hat{\nabla}^2 \hat{\mathbf{u}} + \hat{\mathbf{g}} \hat{T} \frac{Ra}{Re^2 Pr}, \quad (2)$$

$$\frac{\partial \hat{T}}{\partial \hat{t}} = -(\hat{\mathbf{u}} \cdot \hat{\nabla}) \hat{T} + \frac{1}{Pr Re} \hat{\nabla}^2 \hat{T}, \quad (3)$$

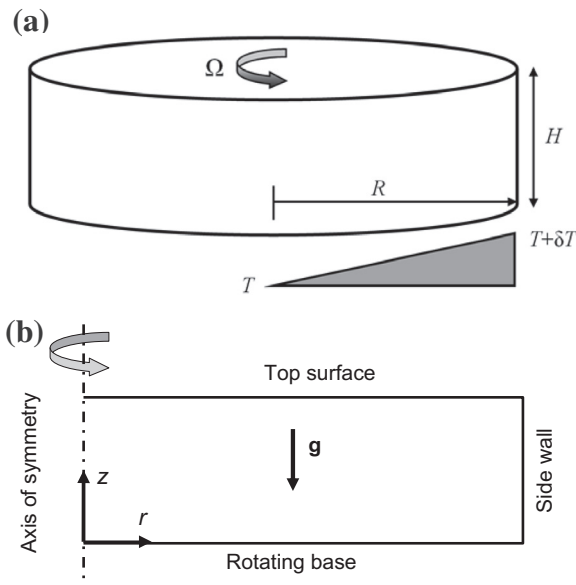


Fig. 1. Schematic representation of the system, showing key symbols and computational domain on the meridional semi-plane.

where $\hat{\mathbf{u}}$, \hat{p} , \hat{t} , Re , Pr , $\hat{\mathbf{g}}$ and \hat{T} are the velocity vector, kinematic static pressure, time, Reynolds number, Prandtl number, a unit vector in the direction of gravity, and temperature, respectively. In Eqs. (1)–(3), lengths have been scaled by R , velocities by $R\Omega$, time by Ω^{-1} , and temperature by δT (the imposed temperature difference across the bottom wall). A Reynolds number characterising the tank rotation rate is defined as

$$Re = \frac{R^2 \Omega}{\nu}, \quad (4)$$

where ν is the kinematic viscosity of the fluid. This Reynolds number relates to the Ekman number characterising the ratio of viscous to Coriolis forces [13]

$$E = \frac{\nu}{2\Omega R^2} = \frac{1}{2Re}. \quad (5)$$

A horizontal Rayleigh number characterising the thermal forcing is given by

$$Ra = \frac{g\alpha\delta TR^3}{\nu\kappa_T}, \quad (6)$$

where g is the gravitational acceleration and κ_T is the thermal diffusivity of the fluid.

In a rotating system the ratio between thermal boundary layer thickness and Ekman layer thickness is important in describing the flow [13]. The square of the ratio between these two thickness scales [1,14] gives

$$Q = \frac{1}{ERa^{2/5}} = \frac{2Re}{Ra^{2/5}}. \quad (7)$$

This ratio accounts for the importance of rotation in horizontal convection. When $Q > O(1)$, the thermal boundary layer is thicker than the Ekman layer, and rotation is important. When $Q < O(1)$, the Ekman layer is thicker than the thermal boundary layer, and frictional dissipation is dominant. For a description of six regimes identified for rotating thermal convection heated non-uniformly from below in terms of Q , the reader is referred to [13]. The effects of rotation and horizontal convection in this system are completely described by any two of Re , Ra and Q . In this paper, both Re and Q are used to describe the effect of rotation on the flow.

The Prandtl number of the fluid is given as

$$Pr = \frac{\nu}{\kappa_T}, \quad (8)$$

and throughout this study $Pr = 6.14$, which approximates water at laboratory conditions. To consider the suitability of this model for implementation in a laboratory setting, a wide range of Rayleigh number ($3.2 \leq Ra \leq 3.2 \times 10^{11}$) and Reynolds number ($0 \leq Re \leq 3200$) are considered in this study.

The Nusselt number, a measure of the ratio of convective to conductive heat transfer, is defined as

$$Nu = \frac{F_T R}{\rho c_p \kappa_T \delta T}, \quad (9)$$

where the heat flux is

$$F_T = \kappa_T \rho c_p \frac{\partial \overline{T}}{\partial z}. \quad (10)$$

Here, $\partial \overline{T} / \partial z$ is the absolute value of the temperature flux integrated over the base.

3. Theoretical analysis

Here we conduct a scaling analysis of the system to provide insight into expected behaviour of the flow. Following previous

studies into plane horizontal convection flows [12,18,19], it is expected that the flow will establish a steady state boundary layer on the forcing boundary. To proceed, consider steady-state ($\partial/\partial t = 0$) axisymmetric ($\partial/\partial \theta = 0$) flow with swirl ($u_\theta \neq 0$) in the cylindrical container of radius R . On the bottom wall, boundary layers (velocity and temperature) are assumed to develop with thickness h , and we consider the case where $h/R \ll 1$.

For convenience, we conduct this analysis in a rotating frame of reference (with angular velocity Ω), and we introduce $u_{\theta,rel}$ for the dimensional azimuthal velocity relative to the rotating reference frame. This requires Coriolis and centripetal terms to be added to the governing equations. With constant rotation about the vertical z -axis, the centripetal contribution is accommodated by adding ($+r\Omega^2$) to the radial momentum equation only. The Coriolis contributions are accommodated by augmenting the radial and azimuthal momentum equations with ($2\Omega u_\theta$) and ($-2\Omega u_r$), respectively. Writing in dimensional form and adopting the aforementioned assumptions, the governing equations become

$$\frac{1}{r} \frac{\partial}{\partial r} (ru_r) + \frac{\partial u_z}{\partial z} = 0, \quad (11)$$

$$u_r \frac{\partial u_z}{\partial r} + u_z \frac{\partial u_z}{\partial z} = -\frac{1}{\rho} \frac{\partial p}{\partial z} + \nu \left[\frac{1}{r} \frac{\partial}{\partial r} \left(r \frac{\partial u_z}{\partial r} \right) + \frac{\partial^2 u_z}{\partial z^2} \right] - \alpha g T, \quad (12)$$

$$u_r \frac{\partial u_r}{\partial r} + u_z \frac{\partial u_r}{\partial z} - \frac{u_{\theta,rel}^2}{r} = r\Omega^2 + 2\Omega u_{\theta,rel} - \frac{1}{\rho} \frac{\partial p}{\partial r} + \nu \left[\frac{1}{r} \frac{\partial}{\partial r} \left(r \frac{\partial u_r}{\partial r} \right) + \frac{\partial^2 u_r}{\partial z^2} - \frac{u_r}{r^2} \right], \quad (13)$$

$$u_r \frac{\partial u_{\theta,rel}}{\partial r} + u_z \frac{\partial u_{\theta,rel}}{\partial z} - \frac{u_r u_{\theta,rel}}{r} = -2\Omega u_r + \nu \left[\frac{1}{r} \frac{\partial}{\partial r} \left(r \frac{\partial u_{\theta,rel}}{\partial r} \right) + \frac{\partial^2 u_{\theta,rel}}{\partial z^2} - \frac{u_{\theta,rel}}{r^2} \right], \quad (14)$$

$$u_r \frac{\partial T}{\partial r} + u_z \frac{\partial T}{\partial z} = \kappa_T \left[\frac{1}{r} \frac{\partial}{\partial r} \left(r \frac{\partial T}{\partial r} \right) + \frac{\partial^2 T}{\partial z^2} \right]. \quad (15)$$

We conduct a scaling analysis of the governing equations as they apply to the forcing boundary layer. In this analysis, r -derivatives are taken to operate over the tank radius, R , z -derivatives are taken to operate over the boundary layer thickness, h , and $h/R \ll 1$. Representative changes in radial and azimuthal velocity, and temperature, across the boundary layers are u_r , $u_{\theta,rel}$ and δT , respectively.

Beginning with the continuity equation, the order of magnitude of each term is

$$O\left(\frac{1}{r} \frac{\partial}{\partial r}\right) = \frac{1}{r} \frac{ru_r}{R} = \frac{u_r}{R}, \quad (16)$$

and

$$O\left(\frac{\partial u_z}{\partial z}\right) = \frac{u_z}{h}. \quad (17)$$

Eq. (11) dictates that these two terms must be equal and opposite. Hence their magnitudes are equal, and

$$u_z \sim u_r \frac{h}{R}; \quad (18)$$

axial velocities are much smaller than radial velocities in the forcing boundary layer.

Considering the temperature transport equation, the advection terms both have orders of magnitude $u_r \delta T/R$. The radial derivative part of the diffusion term is much smaller than the z -derivative

term by a factor of $(h/R)^{-2}$, i.e. $\kappa_T \delta T/R^2 \ll \kappa_T \delta T/h^2$, and is neglected.

Balancing the convection terms with the remaining diffusion term yields $u_r \sim \kappa_T R/h^2$, which can be combined with the continuity result to give

$$u_r \sim \frac{R}{h} u_z \sim \kappa_T \frac{R}{h^2}. \quad (19)$$

At this point it is pertinent to note that these scaling results are identical to those arising from an analysis of planar horizontal convection [12,20], with R replacing base length L . The radial effects cancel in the analysis; a feature that persists through the remainder of the analysis. The exception is a couple of instances where we use $O(r) = R$, which holds at the outer part of the enclosure. This is justified by observation from planar horizontal convection [20,19] that the hot end of the forcing boundary (the outer part in our radial system) is where the convective boundary layer is most prevalent. This result reflects the small- h/R assumption, which means that azimuthal curvature is negligible compared to the boundary layer thickness away from the axis.

It can similarly be shown that the radial-derivative and radial-velocity terms may be eliminated from the radial momentum equation. Likewise the radial-derivative diffusion term may be neglected from the axial momentum equation, and from the azimuthal momentum equation, the radial-derivative part of the diffusion term and the $\nu u_{\theta,rel}/r^2$ term may be neglected. Considering the remaining azimuthal momentum terms demonstrates that if the Coriolis term is in balance with advection and diffusion terms, then $u_{\theta,rel}/R\Omega = \text{constant}$. This means that the relative azimuthal velocity normalised by the tank rotation speed will be constant. Multiplying both sides by ν/R and simplifying gives

$$u_{\theta,rel} \propto Re \frac{\nu}{R}. \quad (20)$$

Hence in an experimental study (with constant tank radius and fluid viscosity), it would be expected that relative azimuthal velocities are proportional to Reynolds number.

More information can be gleaned by cross-multiplying and combining the remaining terms in the momentum equations. Summing the differentiated equations gives us a single equation that permits us to consider the relative magnitude of terms across both the radial and axial momentum equations,

$$\begin{aligned} & \frac{\partial u_r}{\partial r} \frac{\partial u_z}{\partial r} + u_r \frac{\partial^2 u_z}{\partial r^2} + u_z \frac{\partial^2 u_z}{\partial r \partial z} + \frac{\partial u_z}{\partial r} \frac{\partial u_z}{\partial z} + \frac{\partial u_r}{\partial z} \frac{\partial u_r}{\partial r} + u_r \frac{\partial^2 u_r}{\partial r \partial z} \\ & + u_z \frac{\partial^2 u_r}{\partial z^2} + \frac{\partial u_z}{\partial z} \frac{\partial u_r}{\partial z} - \frac{1}{R} 2u_{\theta,rel} \frac{\partial u_{\theta,rel}}{\partial r} \\ & = -\frac{2}{\rho} \frac{\partial^2 p}{\partial r \partial z} + 2\Omega \frac{\partial u_{\theta,rel}}{\partial z} + \nu \frac{\partial^3 u_z}{\partial r \partial z^2} + \nu \frac{\partial^3 u_r}{\partial z^3} - \alpha g \frac{\partial T}{\partial r}. \end{aligned} \quad (21)$$

Noting that $u_r \sim \kappa_T R/h^2$ and $u_z \sim \kappa_T/h$, we find that the axial momentum advection terms and diffusion term are negligibility small compared with their radial-momentum counterparts (consistently h^2/R^2 the size), and may therefore be discarded.

If the buoyancy is in balance with advection or diffusion terms, then we recover $PrRa(h/R)^5 \propto \text{constant}$, so $h/R \propto (PrRa)^{-1/5}$. Hence for a constant Prandtl number,

$$\frac{h}{R} \propto Ra^{-1/5}. \quad (22)$$

This scaling of the normalised boundary layer thickness as being proportional to $Ra^{-1/5}$ is identical to that reported by Rossby [12,18] for planar horizontal convection.

A result of some importance (to be discussed later) arises from a balance between buoyancy and the radial-momentum Coriolis term. This balance gives $PrRa(h/R)^5 \propto R\Omega u_{\theta,rel}/u_r^2$, or $u_{\theta,rel}/u_r \propto PrRa(u_r/R\Omega)(h/R)^5$. Hence the ratio of relative azimuthal velocity

to radial velocity is proportional to the product of radial velocity normalised by tank velocity (the dimensionless radial velocity in our simulations to follow), and $PrRa(h/R)^5$. Given Eq. (22), then $u_{\theta,rel}/u_r \propto u_r/R\Omega$.

Further insight may be gained by taking the difference between the remaining terms in the cross-differentiated radial and axial momentum equations to eliminate pressure, which yields

$$\frac{2}{r} \left(u_r \omega_\theta + u_\theta \frac{\partial u_\theta}{\partial r} \right) + 2\Omega \frac{\partial u_\theta}{\partial z} = -v \frac{\partial^2 \omega_\theta}{\partial z^2} - \alpha g \frac{\partial T}{\partial r}, \quad (23)$$

where the azimuthal component of vorticity, $\omega_\theta = \partial u_r/\partial z - \partial u_z/\partial r$, and the continuity relation has been employed to simplify the left-hand side.

The order of magnitude of vorticity can be deduced from its velocity derivative components,

$$O(\omega_\theta) = \max \left[O\left(\frac{\partial u_r}{\partial z}\right), O\left(\frac{\partial u_z}{\partial r}\right) \right] = \max \left[\frac{u_r}{h}, \frac{u_r}{h} \left(\frac{h}{R}\right)^2 \right] = \frac{u_r}{h} \sim \kappa_T \frac{R}{h^3}, \quad (24)$$

so the $\partial u_z/\partial r$ term is negligible.

Recalling that $u_r \sim \kappa_T R/h^2$ and $u_z \sim \kappa_T/h$, $u_{\theta,rel}/u_r \propto u_r/R\Omega$, evaluating the order of magnitude of each term, multiplying all results by $h^5/R\kappa_T^2$ and simplifying produces some interesting results: the buoyancy and diffusion terms are of order Pr , and the first advection term of order 1. However, the remaining terms, $(2/r)u_{\theta,rel}\partial u_{\theta,rel}/\partial r$ and $2\Omega\partial u_{\theta,rel}/\partial z$, each go as different functions of u_r and $u_{\theta,rel}$. Taking the ratio of their orders of magnitude and solving for $u_{\theta,rel}$ yields

$$u_{\theta,rel} \propto ReRa^{1/5}v/R. \quad (25)$$

We have earlier determined a scaling for u_r , and combining these yields

$$\frac{u_{\theta,rel}}{u_r} \propto PrReRa^{-1/5}. \quad (26)$$

This expression demonstrates that increasing either the Prandtl number or Reynolds number, or decreasing Rayleigh number, each lead to an increase in the ratio $u_{\theta,rel}/u_r$. We will later show that Eq. (26) serves to explain a stabilizing effect with increasing Reynolds number observed in our simulations.

Insight into the allowable shapes of the thermal and velocity boundary layers may be obtained by evaluating the reduced governing equations at the bottom wall (where $\mathbf{u} = 0$), which gives

$$\frac{\partial u_z}{\partial z} = 0, \quad (27)$$

$$\frac{1}{\rho} \frac{\partial p}{\partial r} = r\Omega^2 + v \frac{\partial^2 u_r}{\partial z^2}, \quad (28)$$

$$\frac{1}{\rho} \frac{\partial p}{\partial z} = -\alpha gT, \quad (29)$$

$$\frac{\partial^2 u_{\theta,rel}}{\partial z^2} = 0, \quad (30)$$

$$\frac{\partial^2 T}{\partial z^2} = 0. \quad (31)$$

In particular, Eqs. (30) and (31) show that there must be zero curvature in vertical profiles of both azimuthal velocity and temperature at the bottom wall.

Finally, as described earlier, the cylindrical components become negligible in the scaling analysis, so collecting the preceding scaling relations provides results consistent with the forcing boundary layer scalings derived for planar horizontal convection [12,20], i.e.

$$\frac{h}{R} \sim Ra^{-1/5}, \quad (32)$$

$$\frac{u_r R}{\kappa_T} \sim Ra^{2/5}, \quad (33)$$

$$\frac{u_z R}{\kappa_T} \sim Ra^{1/5}. \quad (34)$$

By combining Eqs. (9) and (10), a scaling for Nusselt number is found to be

$$Nu \sim Ra^{1/5}, \quad (35)$$

which follows from Eq. (32) and $Nu \sim (\delta T/h)R/\delta T \sim (h/R)^{-1}$.

We can recover Q to demonstrate its relevance to the present system by taking the square of the ratio of Eq. (32) to the Ekman layer scale (\sqrt{E}) , i.e.

$$\left(\frac{h/R}{\sqrt{E}}\right)^2 = \frac{Ra^{-2/5}}{E} = Q. \quad (36)$$

In this paper, the predicted scalings arising from this analysis will be tested using time-dependent, axisymmetric numerical simulations described in the sections to follow.

4. Numerical methodology

A nodal spectral-element method is used to discretise the governing flow and energy Eqs. (2) and (3) in space, and a third-order scheme based on backwards differentiation is employed for time integration [21]. The spectral element method is similar to the finite element method, in that the fluid domain is divided into a mesh of individual elements. However, instead of employing a low-order (e.g. linear) basis over each element, a high-order polynomial basis is instead used, permitting very rapid convergence with increasing polynomial degree [21]. An in-house solver is used, and the governing equations are solved in cylindrical coordinates [22,23].

4.1. Spatial and temporal discretisation

The computational domain in the $z-r$ plane is broken up into quadrilateral elements. A rectangular mesh comprising 1560 elements was constructed to discretise the meridional semi-plane. Care was taken to ensure that the flow was resolved in the vicinity of the walls, and particularly the heated boundary, with coarser mesh spacing in the interior. A grid independence study determined that integrated Nusselt numbers were independent of resolution to better than 0.1% with an element polynomial degree of 5, which is used hereafter.

For time integration of Eqs. (2) and (3), the advection/convection terms are concurrently solved explicitly, followed by a projection of the velocity field onto a divergence-free space, and finally implicit solves for velocity components and temperature. This procedure extends the backwards-differentiation algorithm of [21] to the coupled temperature equation. The temperature transport formulation of the present code has been validated in studies on heat transfer enhancement in duct flows [24–26].

5. Results and discussion

Results are presented in three subsections. Firstly, Nusselt numbers as functions of Reynolds number and Rayleigh number are reported. This is followed by consideration of the development of unsteady flow, and interrogation of the boundary-layer velocity profiles. Finally, the temperature and azimuthal velocity fields in the enclosure are presented.

5.1. Nusselt number scalings and flow regimes

Here the heat transfer through the base of the enclosure is considered. For this enclosure, the dependence of Nusselt number on the Rayleigh number for different Reynolds numbers is shown in Fig. 2(a). In Fig. 2(b), gradients of the log–log data are plotted. Linear regions of the data shown in Fig. 2(a) indicates a power law relationship $Nu \sim Ra^\gamma$, where the log–log gradient gives γ . Accompanying Fig. 2 is Fig. 3, which quantifies Q for the Nu – Ra – Re data computed in this study. A number of observations can be made in relation to the data in Fig. 2. Consistent with experiments and simulations of planar horizontal convection flows, for a given Reynolds number the Nusselt number passes through three different regimes as Rayleigh number is increased. For small Rayleigh numbers, it is found that the Nusselt number is independent of both Rayleigh number and Reynolds number. In this regime, which is referred to here as regime I, diffusion dominates, and the flow lacks a distinct boundary layer adjacent to the bottom boundary. At high Rayleigh numbers, the radially forced horizontal convection dominates and the Nusselt number recovers its Reynolds-number independence, while exhibiting a strong power-law dependence on Rayleigh number with an exponent very close to the 1/5 predicted from theory (see Eq. (35)). This convection-dominated regime is referred to as regime III. Connecting regimes I and III is a transitional regime (regime II) where the Nusselt number increased from its regime I value towards the convection-dominated regime.

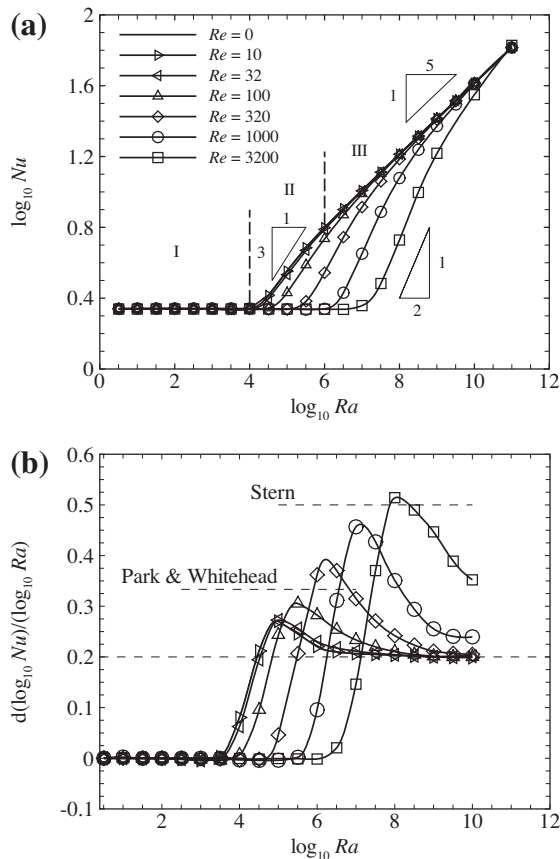


Fig. 2. (a) A plot of $\log_{10}Nu$ against $\log_{10}Ra$ for different Reynolds number as indicated. Akima splines are fitted to the data for guidance. I, II and III identify the diffusion-dominated, intermediate, and convection-dominated regimes, respectively. (b) A plot of gradient of the curves in (a), calculated using finite difference. Gradient indicators (a) and dashed lines (b) show the theoretical scaling for convection-dominated flow ($Ra^{1/5}$), plus scalings incorporating the effect of rotation adapted from Park and Whitehead ($Ra^{1/3}$) and Stern ($Ra^{1/2}$).

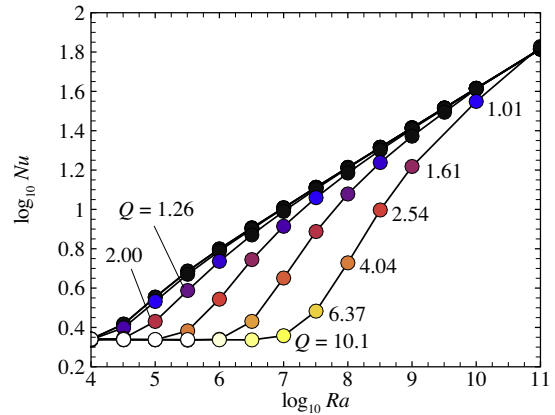


Fig. 3. A plot of $\log_{10}Nu$ against $\log_{10}Ra$ for different Reynolds numbers reproducing the data from Fig. 2(a) shaded by $\log_{10}(Q)$. Black symbols show $Q < 1$, and dark through to white shading covers the range $1 \leq Q \leq 32$ on a logarithmic scale. White shading is used for all $Q \geq 32$. For guidance, selected symbols are labelled for their Q -values.

The threshold between regimes I and II demonstrates a dependence on Reynolds number, and hence on the rate of rotation of the system. At $Re = 0$, the threshold between regimes I and II occurs at $Ra \approx 10^4$. Modest rotation rates up to $Re \approx 3 \times 10^1$ exhibit a virtually indistinguishable threshold Rayleigh number. However, at larger rates of rotation the threshold is delayed to progressively larger Rayleigh numbers. The explanation for this can be deduced from the thickness of the thermal boundary layer. In the absence of rotation, this layer follows Rossby’s scaling, $h/R \sim Ra^{-1/5}$ [12], which for a Rayleigh number of 10^4 and the present aspect ratio $H/R = 0.4$ corresponds to a thickness of approximately 40% of the enclosure height, or $h/H \approx O(1)$. The effect of rotation is expected to become significant beyond $Q = O(1)$, where the scalings proposed by Stern [2] and Park and Whitehead [1] each predict the thermal layer thickens to increase with rotation rate. The respective scalings are summarised in [14] and can be written in the present nomenclature as $h/R \sim Q^{3/4}Ra^{-1/5}$ and $h/R \sim Q^{1/3}Ra^{-1/5}$. Noting that $h/R = (h/H)(H/R)$, these scalings demonstrate that $h/H \sim Q^\gamma Ra^{-1/5}(H/R)^{-1}$, where $\gamma = 3/4$ or $1/3$, depending on which expression is used. In other words, for a given aspect ratio, a higher Rayleigh number is required at higher rotation rates (higher Q) to reduce the thickness below the $h/H = O(1)$ required to enter regime II.

The question as to which of these predicted scalings, if any, are relevant to the present system will be discussed shortly; in the meantime the role of Q on the threshold is considered. Here the regime I threshold is constant at $Ra \approx 10^4$ for $Re \leq 32$, which corresponds to $Q < 1.6 \approx O(1)$. By $Re = 100$, where a noticeable delay in the threshold Rayleigh number begins to be seen, at $Ra \approx 10^4$ the rotation parameter $Q = 5$ which is greater than $O(1)$, demonstrating the influence of rotation on the delay of this threshold Rayleigh number.

Having established the importance of h/H in delineating diffusive and convective regimes in horizontal convection flow, it is pertinent to discuss the role of the enclosure aspect ratio on these regimes. Sheard and King [27,19] demonstrated that for planar horizontal convection, the Nu – Ra trends were unaffected by aspect ratio for larger aspect ratios, and only aspect ratios $H/L \leq 1/3$ exhibited an appreciable deviation from the H/L -independent data. Here again the importance of h/H was observed: smaller aspect ratios confined the flow, bringing the opposite boundary into proximity with the forcing boundary layer. As with the cases with larger Reynolds number described here, in that study a higher Rayleigh number was required to overcome the diffusion-dominated

regime. In [27,19], a feature of the Nu – Ra trend at larger aspect ratios was that no appreciable spike in gradient was observed in their regime II; rather, the gradient smoothly increased from zero to the $1/5$ scaling. In the present study, the low-Reynolds-number cases exhibit a small gradient spike in regime II, which suggests that the enclosure is modestly affected by aspect ratio. It is therefore possible that enclosures with a larger aspect ratio might exhibit slightly different thresholds between regimes to those reported here. Conversely, smaller aspect ratios would produce progressively larger deviations of the thresholds to higher Rayleigh numbers due to the aforementioned vertical confinement of the horizontal flow.

The scaling in the convection-dominated regime III is further illustrated by the plot of the gradients of the trends in Fig. 2(b). The gradient data was found by interpolating Akima spline fits to the data and determining the gradients through finite differences. Regime I is identifiable by gradients of approximately zero; regime III by gradients of approximately $1/5$, and regime II by the range of intermediate Rayleigh numbers where a spike in gradient is produced corresponding to the elevation in Nusselt number towards the $Ra^{1/5}$ regime. Having established that the onset of regime II is delayed by higher rotation rates, it becomes apparent that the Reynolds-number-dependence observed in the Nu – Ra data in regime II is due to the effect of rotation, which is characterised by Q . To elucidate, Fig. 3 displays the data from Fig. 2(a) with symbols shaded by values of Q . It is seen that progressively higher Reynolds numbers result in progressively higher values of Q being reached within regime II, and that consistently as each data set approaches the collapsed regime III trend, $Q \rightarrow O(1)$. Consistently, regime III is characterised by cases with $Q < O(1)$.

To gain further insight into how the Nusselt number results presented in Fig. 2(a) vary against the scalings suggested by Park and Whitehead [1] and Stern [2], the reciprocal of the respective thermal boundary layer scalings taken from the summary provided in [14] result in Nusselt number scalings of $Nu \sim Q^{-1/3}Ra^{1/5}$ and $Nu \sim Q^{-3/4}Ra^{1/5}$, respectively. Given that these scalings have been developed for flows with $Q > 1$, they should be tested against our data corresponding to regime II, which satisfies this criterion. The data in Fig. 2 is recast against each of these scalings in Fig. 4. The proposed scalings are valid where a unit gradient is produced in the plots. In each of the plots in Fig. 4, the data has been partially collapsed on the horizontal axis. At the left, the constant Nusselt numbers of regime I can be seen in both figures, then the departures to regime II occur, and finally, each of the data sets reverts to a gradient consistent with the $Ra^{1/5}$ scaling of regime III, but the regime III data no longer collapses due to the change in the parameter plotted on the horizontal axis. These plots further reinforce that regime III corresponds to data with $Q < 1$.

Prior to considering the implications of the data presented in Fig. 4, consideration is given to the underlying Reynolds number and Rayleigh number scalings suggested by the Nusslet number scalings of [1,2]. Substituting Eq. (7) into the respective formulae results in

$$Q^{-1/3}Ra^{1/5} \propto Re^{-1/3}Ra^{1/3}, \quad (37)$$

from the Park and Whitehead scaling, and

$$Q^{-3/4}Ra^{1/5} \propto Re^{-3/4}Ra^{1/2}, \quad (38)$$

from the Stern scaling. The slopes corresponding to the Rayleigh-number scalings described in these relations are included in Fig. 2(a) for guidance. It can then be noted that data at high Reynolds numbers appears to follow a scaling of $Ra^{1/2}$ as suggested by Stern's relationship, while at lower Reynolds numbers, a scaling of $Ra^{1/3}$ consistent with [1] is instead observed.

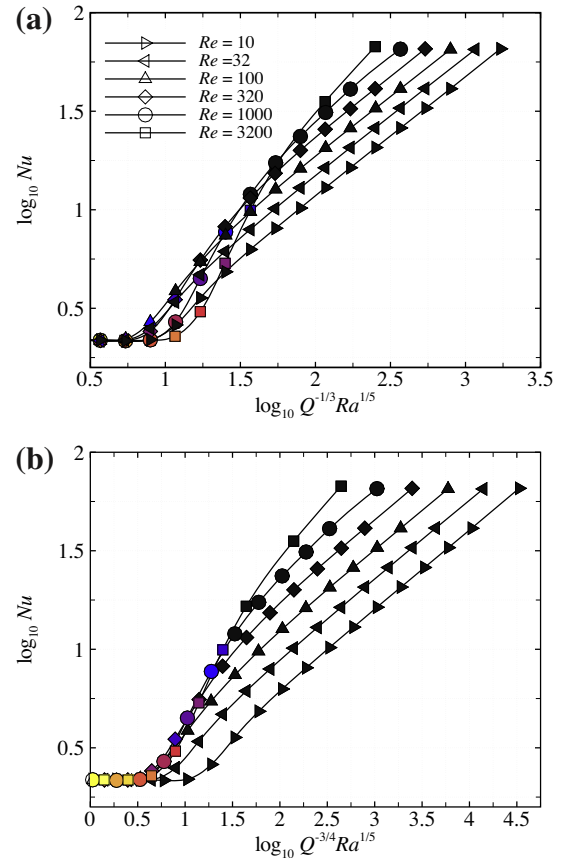


Fig. 4. A plot of $\log_{10}Nu$ against $\log_{10}Q^{-1/3}Ra^{1/5}$ (a) and $\log_{10}Q^{-3/4}Ra^{1/5}$ (b) for different Reynolds following Park and Whitehead [1] and Stern [2], respectively. The data are shaded by $\log_{10}(Q)$ as per Fig. 3.

The boundaries between regimes are now discussed, using information revealed from Fig. 4. Considering firstly the boundary between regimes I and II, Fig. 2 demonstrates that at low Reynolds numbers ($Re \lesssim 32$) the boundary lies at $Ra \approx 10^4$. With increasing Reynolds number, rotational effects delay the onset of this regime by thickening the thermal boundary layer [14], thus requiring progressively higher Rayleigh numbers to overcome this effect and form the distinct boundary layer on the bottom wall occupying regime II. Fig. 4 can be used to determine expressions for the I–II regime boundary at higher rates of rotation. In Fig. 4(a), it can be seen that over $32 \lesssim Re \lesssim 320$, the data exhibits a departure from the regime-I Nusselt number at $\log_{10}Q^{-1/3}Ra^{1/5} \approx 0.75$. Substituting Eq. (7) and solving gives

$$Ra_{I-II} = 2 \times 10^{9/4} Re \approx 356 Re. \quad (39)$$

To test this relationship against Figs. 2 and 3, we substitute $Re = 100$ into the expression. The result yields $\log_{10}Ra = 4.6$, consistent with the corresponding behaviour in Fig. 2. Using these values with Eq. (7) yields $Q = 3.0$ at the threshold, which is consistent with the trend in Q values indicated in Fig. 3.

It was earlier described that for an enclosure with $H/R = 0.4$, the transition from regime I to II occurs when $h/H \approx 0.4$. Using the thickness scaling expression from [1] and substituting the threshold value $Q^{1/3}Ra^{-1/5} \approx 10^{-0.75}$ yields $h/H \sim 0.45$. This indicates that at moderate rotation rates the boundary layer thickness is slightly greater at the threshold of regime II.

In Fig. 4(b), $Re \gtrsim 100$ data sets depart from the regime-I Nusselt number at a tightly collapsed value of $\log_{10}Q^{-3/4}Ra^{1/5} \approx 0.5$. Substituting Eq. (7) and solving gives

$$Ra_{I-II} = 2^{3/2} \times 10Re^{3/2} \approx 28.3Re^{3/2}. \quad (40)$$

Applying this relationship to $Re = 3200$ yields a threshold at $\log_{10}Ra = 6.7$ with $Q = 13.3$, consistent with the data in Figs. 2 and 3. Geophysically relevant oceanic values of the rotation parameter are beyond $Q = O(100)$ [14], while the highest values found in the rotation-affected convection regime in the present study are $Q = O(10)$. Nevertheless, the tight collapse at higher Reynolds numbers seen in Fig. 4(b) suggests that Stern’s scaling is appropriate for higher rotation rates. Recalling the assumptions by which the scalings of Park and Whitehead and Stern were constructed (see Section 1 and [14]), the findings in Fig. 4 therefore imply that with increasing rotation rate, the balance between advection and vertical diffusion in the buoyancy equation that underpins non-rotating flows carries over to moderately rotating flows, but that this ultimately gives way to Stern’s energy equation balance at higher rates of rotation.

Using the thickness scaling expression from Stern and substituting the threshold value $Q^{3/4}Ra^{-1/5} \approx 10^{-0.5}$ yields $h/H \sim 0.79$. This reveals that at high rotation rates the boundary layer thickness is significantly greater at the threshold of regime II, and that the effect of increasing rotation rate is to increase the boundary layer thickness at the onset of the convective regimes.

The threshold between regimes II and III denotes the boundary between convective flows that are influenced by rotation (regime II) and those that are not (regime III). This threshold is elucidated by Fig. 3, where it is shown that data with $Ra \gtrsim 10^{5.5}$ and $Q < O(1)$ collapse to the horizontal convection trend following the expected $Ra^{1/5}$ scaling. Hence $Q = 1$ is adopted to define the threshold at higher Reynolds numbers, while at lower Reynolds numbers the threshold is described by $Ra \gtrsim 10^{5.5}$. The intercept between these trends occurs at $Re \approx 79$.

The aforementioned regime threshold expressions are combined to construct the regime map shown in Fig. 5. This map reinforces that for small $Q < O(1)$ the thresholds are independent of Reynolds number. Additionally, the interesting regime of rotation-influenced convective flow (regime II) occupies an increasing range of Rayleigh numbers with increasing Reynolds number, thanks to the upper and lower bounding Rayleigh numbers going with $Re^{5/2}$ and $Re^{3/2}$, respectively.

5.2. Emergence of unsteady flow

Attention is now turned to the question of the stability of the flow. The development of unsteady flow in horizontal convection is important in the context of the overarching debate over the role of turbulence in horizontal convection. This question is also related

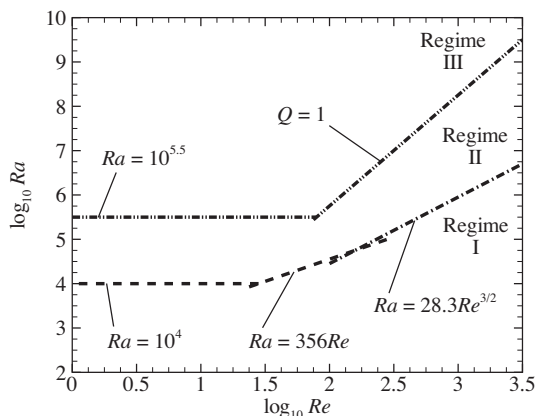


Fig. 5. Map showing regime boundaries over the Ra – Re parameter space.

to whether a horizontal convection mechanism alone would be sufficient to drive overturning circulation in Earth’s oceans. Paparella and Young [28] proposed the so-called “anti-turbulence theorem” in which it was argued that horizontal convection was inherently non-turbulent. Specifically, they showed that for a fixed Prandtl number, the volume-averaged energy dissipation goes to zero as both kinematic viscosity and thermal diffusivity go to zero. Siggers et al. [29] used a variational approach to determine an upper bound on Nusselt number scaling at the 1/3 power of Rayleigh number in non-rotating planar horizontal convection, which was substantially higher than the 1/5 scaling predicted and observed in stable horizontal convection [12,20]. While the suggested upper bound could have been exaggerated by insufficiently tight bounds in the analysis, this work did nonetheless suggest the possibility that another flow regime (such as instability or turbulent convection) could result in a higher scaling exponent. Establishing the correct exponent for high-Rayleigh number horizontal convection is important when extrapolating to geophysical scales. Sheard and King [27,19] reported high-resolution numerical simulations using a high-order spectral-element method in which the onset of unsteady flow triggered an increase in the Nu – Ra scaling exponent from 1/5 in the stable regime to ≈ 0.3 . Calculations extrapolating to geophysical scales, i.e. $Ra = O(10^{31})$ [29,30], reveal that the 1/5 scaling produces a poleward oceanic heat transport some three orders of magnitude below the oceanic value, but that the 0.3 scaling achieves a heat transport consistent with that in Earth’s oceans. Therefore the development of unsteady flow and turbulence in horizontal convection is a critical question.

Scotti and White [31] revisited Paparella and Young’s anti-turbulence theorem using direct numerical simulation of horizontal convection at Rayleigh numbers up to $Ra = 10^{10}$ arguing that the anti-turbulence criterion was too restrictive and that horizontal convection did indeed become turbulent. In contrast, numerical simulations up to $Ra = 10^{11}$ reported by Ilıcak and Vallis [32] suggested that in the absence of mechanical forcing, horizontal convection was insufficient to drive a significant overturning at high Rayleigh numbers despite the interior flow being unsteady. However, Gayen et al. [33] analysed the energy budget of three-dimensional direct numerical simulations of horizontal convection for Rayleigh numbers up to $Ra = 10^{12}$ and concluded that dissipation rate is not an indicator of the strength of the circulation, and that horizontal convection was sufficient to drive energetic circulation.

There remains quite some disagreement over the nature of instability and onset of unsteady flow leading to turbulence in horizontal convection, not least due to the high resolution needed to accurately capture the forcing boundary layer and vertical plume region of the flow, whose scales decrease with increasing Rayleigh number. In [27,19] the onset of unsteady flow was found to consistently emerge at $Ra = O(10^9)$, a value supported by the subsequent simulations of [30] that were progressed well beyond this value and up to $Ra = 10^{12}$. How, then, is the development of unsteady flow affected by rotation and the radial thermal forcing in the present cylindrical system?

The onset of unsteady flow in the present system is delayed by approximately an order of magnitude in Rayleigh number when compared to planar non-rotating horizontal convection. While many of the simulations exhibit some unsteady features such as mushroom plume eruption from the forcing boundary during the transient phase, upon reaching thermal equilibrium, a time-periodic unsteadiness is first detected at $Ra = 10^{10}$ for all Reynolds numbers considered here ($0 \leq Re \leq 3200$). Stable steady-state equilibrium flows are produced for all lower Rayleigh numbers computed in this study ($Ra \leq 3.2 \times 10^9$). Rotation is therefore not found to significantly affect the onset of unsteady flow over this Reynolds number range; this is supported by the Nusselt number

data in Fig. 2, where at $Ra = 10^{10}$, all of these Reynolds numbers produce Nusselt numbers at of very close to the Reynolds-number-independent regime III. Indeed, Fig. 3 further demonstrates that at the highest Reynolds number, $Q = 1.01$ at this Rayleigh number, verifying that the rotation rate is too small to be significant. It remains an open question as to what the effect of further increases in Reynolds number would be on the onset of unsteady flow. However, it could be expected that the onset would be further delayed to higher Rayleigh numbers due to higher rotation rates thickening the thermal boundary layer and delaying the onset of the radial convective flow. Overriding this, though, is the potential for non-axisymmetric flow such as baroclinic instability, which is suppressed in the present axisymmetric simulations. As stated in Section 1, the linear stability analysis of Hignett et al. suggested a critical value of the rotation parameter $Q_c \approx 3.4$ beyond which baroclinic instability would be produced. Barkan et al. [14], who employed a Prandtl number $Pr = 7$, estimated for their system a critical value $Q_c = 2.63$.

Hignett et al.'s expression for critical rotation rate is

$$Q_c \geq \left(Pr \left(\frac{R_d}{R} \right)^2 \right)^{-4/11}, \quad (41)$$

where R_d is the Rossby radius of deformation. Noting that the enclosure radius must be large enough to contain several Rossby radii of deformation (i.e. $R/R_d \geq 10$) [14], this yields a critical rotation rate of $Q_c \geq 2.76$ with the present Prandtl number. Referring to Fig. 5, it would therefore be expected that baroclinic instability would be found at higher rotation rates within the regime II band, and that at moderate Reynolds numbers, baroclinic instability may emerge at lower Rayleigh numbers than the $Ra = O(10^{10})$ at which instability is seen in the non-rotating regime.

The Rossby radius of deformation $R_d = NH/f$, where the Brunt–Väisälä frequency $N \equiv \sqrt{-(g/\rho)(d\rho/dz)}$, and $f = 2\Omega$ is the Coriolis parameter. Under the non-dimensionalisation applied to the present system, Hignett et al.'s criterion can be recast as

$$Q_c \geq \left(\left(\frac{H}{R} \right)^2 \frac{Ra}{Re^2} \frac{dT}{dz} \right)^{-4/11}. \quad (42)$$

In the present simulations, the temperature field varies both radially and axially, and as later shown, very different fields are found across the different flow regimes. Nevertheless, to provide an approximate indication of where baroclinic instability might emerge, the mean vertical temperature gradient was calculated from each simulation, and this was substituted into Eq. (42). Here the Rossby radius of deformation is obtained from the computed temperature fields, hence unstable values are taken as those satisfying $Q_c \geq 2.76$. Both of these estimates demonstrated that with increasing Reynolds number, the range of Rayleigh numbers potentially supporting baroclinic instability increased. However, the threshold calculated from the computed temperature fields corresponds to a higher value of Q than that obtained assuming $R/R_d \geq 10$. For instance, at $Re = 320$, the computed $R/R_d = 10$ threshold occurs at $Q = 6.9$, and for $Re = 1000$, at $Q = 7.7$.

The delay in onset of unsteady flow in the present system can be explained by the fact that the boundary-layer flow moving radially outward experiences two effects not seen in the planar convection case: the azimuthal spreading with increasing r may produce one or both of a reduction in height (and hence boundary layer thickness) or a reduction in velocity, as a result of the incompressibility constraint. This concept is depicted in Figs. 6 and 7 a comparison is made for boundary layer thickness and maximum radial/horizontal velocity in the boundary layer between radial and planar horizontal convection. The test case had $Re = 0$ and

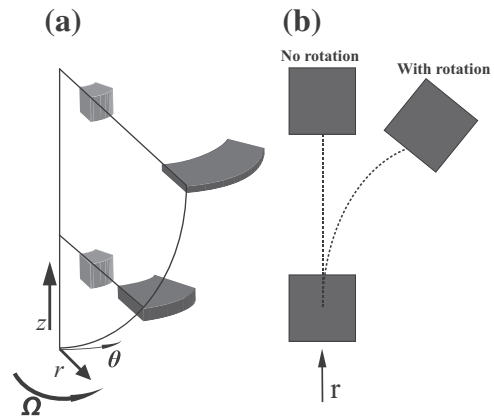


Fig. 6. (a) Schematic representation of the azimuthal spreading of fluid elements within the forcing boundary layer. (b) Viewed from above, this illustration depicts the Coriolis effect serving to deflect fluid elements azimuthally opposite the direction of rotation (which is counter-clockwise in this depiction).

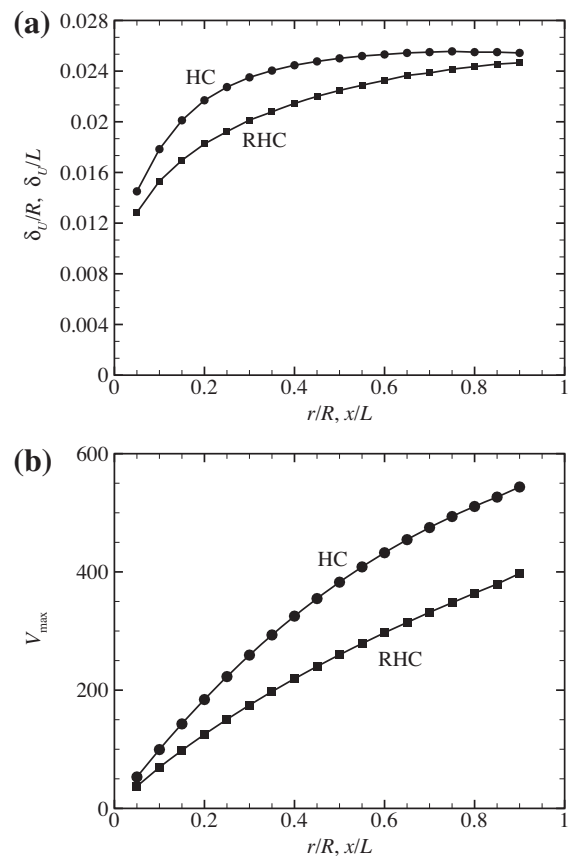


Fig. 7. Plot of (a) velocity boundary layer thickness and (b) maximum horizontal velocity in the boundary layer for plane horizontal convection ("HC") and radial horizontal convection ("RHC") as functions of horizontal location along the base for $Re = 0$ and $Ra = 10^8$.

$Ra = 10^8$, and data is plotted over the full length of the forcing boundary.

In both the planar and radial horizontal convection cases, the velocity boundary layer thickness follows a similar trend, approximately doubling in thickness from the cold to the hot end of the enclosure. Moving from the cold to the hot end, the planar case experiences a more rapid growth than the radial case initially, and plateaus beyond $x/L \approx 0.7$. The boundary layer thickness for

the radial case is initially approximately 10% below that of the planar case, and as it grows more gradually over the cooler part of the base (up to $r/R \approx 0.3$), the discrepancy widens to approximately 20%. Beyond this point the gap narrows again to less than 4% at the hot end of the base ($r \rightarrow R$), so it is apparent that the radial spreading does not lead to a continuous departure of the boundary-layer thickness to progressively smaller values than measured in the planar case. However, such a behaviour is observed when considering the maximum radial/horizontal velocity in the forcing boundary layer. Near the cold end of the base, the planar and radial cases each exhibit similar and small maximum velocities. Moving towards the hot end, the planar case experiences a consistently more pronounced maximum velocity increase compared with the radial case. Hence for a given Rayleigh number, the azimuthal spreading in the cylindrical system serves to decrease the peak boundary layer velocities (and subsequently reduce the velocity shear and horizontal thermal transport in the boundary layer). To produce a similar convective boundary layer velocity profile in the radial case, a higher Rayleigh number is required compared to the planar case: it would therefore be expected that a temporally unstable regime would exist for the radial horizontal convection system at a Rayleigh number beyond $Ra = 10^{10}$.

To confirm that the onset of unsteady flow at equilibrium was not significantly affected by numerical resolution, additional simulations were computed with element orders ranging between 4 and 8, with no variation in the steady and time-periodic behaviours seen at the Rayleigh numbers bracketing the transition. Further simulations were conducted at $Re = 0$ up to $Ra = 3.2 \times 10^{11}$, which found the same sequence of transitions as our corresponding planar horizontal convection simulations find; a transition from steady to time-periodic flow, followed by a subsequent transition from time-periodic to irregular time-dependent flow at a Rayleigh number approximately one order of magnitude higher than the original unsteady transition Rayleigh number is found. The difference is that the corresponding critical Rayleigh numbers are higher in the radial forcing system than for planar horizontal convection.

5.3. Velocity and thermal boundary layers

From Fig. 2, it can be clearly shown that at intermediate Rayleigh numbers (between the diffusion- and convection-dominated regimes, Nusselt number decreases with increasing Reynolds number. An analogous behaviour has been observed for Rayleigh-Bénard convection in a rotating system (see Ref. [4] and references therein). In that system an enhancement of heat transfer is found for modest rotation rates compared to non-rotating Rayleigh-Bénard convection ascribed to Ekman pumping transporting fluid from the top and bottom walls. However, this effect was suppressed at higher rotation rates. In another example of the effect of rotation in suppressing convective flow, Chandrasekhar [34], Chandrasekhar and Elbert [35] considered convection above a rotating plate heated from below. In those studies, a linear stability analysis demonstrated that higher rotation rates served to inhibit the onset of convective flow, and with this also came a reduction in the heat transport. A point of contrast between that system and horizontal convection flows is that horizontal convection is present for any finite thermal forcing [20] whereas in systems with a vertical heat flux, convective flow only develops beyond some critical Rayleigh number. To discuss the reduction in Nusselt number with increasing Reynolds number in the present system, we refer to Eq. (26). This ratio is key to the observed reduction in Nusselt number with increasing Reynolds number. The increase in $u_{\theta,rel}/u_r$ with increasing Reynolds number describes a shift in the boundary layer velocity from the radial direction (maximising Nusselt number due to the effect of carrying the cooler fluid at small

radii over the hotter outer parts of the base), towards the azimuthal direction, and as there is no temperature change in the azimuthal direction, base heat transfer regresses to diffusion, resulting in the reduction in Nusselt number. Hence progressively higher Reynolds numbers require progressively higher Rayleigh numbers to compensate for this effect, explaining the delayed onset of the intermediate and convective regimes.

Velocity and temperature profiles extracted at a location towards the hotter part of the base (we choose $r/R = 0.9$) may be interrogated to verify predictions from the scaling analysis presented in Section 3. Fig. 8 shows vertical profiles of u_r , $u_{\theta,rel}$ and T at Rayleigh numbers of $Ra = 10^9$ and $Ra = 10^6$. In this figure, dimensional velocities are normalised by a viscous velocity scale (ν/R) rather than the tank rotating velocity scale ($R\Omega$) to provide a more intuitive picture of the behaviour from the perspective of laboratory experimentation (where typically R and ν would be fixed, while Ω and δT would be altered to control Re and Ra , respectively).

Consider firstly the $Ra = 10^9$ data shown in Fig. 8(a). This Rayleigh number is chosen as from Fig. 2 it is observed that for $Re \lesssim 1000$, the flow is well into the convection-dominated regime, and there is a limited variation in Nu with Re . In this case, the radial velocity displays minimal sensitivity to changing Reynolds number: the radial flow follows the thermal horizontal convection forcing. Further evidence of the dominant role of thermal forcing is revealed in the $u_{\theta,rel}$ data, which within the boundary layer is consistently much smaller than the corresponding radial velocities. Further, recall that Eq. (25) states that $u_{\theta,rel}$ is proportional to Reynolds number: this is reflected here by the observed increase in $u_{\theta,rel}$ within the boundary layer as Reynolds number is increased. The relative temperature plot demonstrates that near the wall a negative temperature gradient is produced; this arises from the transport of cooler fluid from smaller r over the hotter wall regions at larger r . Across the three figures a consistently thin boundary layer is evident, confined approximately to the bottom 5% of the enclosure. Further from the base, occupying approximately the upper 60% of the enclosure, velocity and temperature profiles become almost independent of z . This corresponds to the expected diffusive discharge of fluid from the vertical plume at the hot end of the enclosure [3]. With reference to the regime map in Fig. 5, these four Reynolds numbers all correspond to cases with $Q < 1$, and therefore they all lie within the convection-dominated regime III.

Secondly, the profiles at the lower Rayleigh number $Ra = 10^6$ shown in Fig. 8(b) are considered. At this Rayleigh number, Fig. 2 demonstrates that there is a strong Reynolds number dependence on Nusselt number: as Reynolds number varies from $Re = 10$ to 1000 the flow transitions from convection-dominated through to diffusion-dominated behaviour. The first observation to draw is that, as expected, the boundary layers are substantially thicker than at $Ra = 10^9$. Eq. (22) predicts that as Ra increases by a factor of 10^3 from $Ra = 10^6$ to 10^9 , the boundary-layer thickness should reduce by a factor of approximately 4.0. In fact, the measured radial velocity profiles from Fig. 8(a) and (b) exhibit thicknesses that differ by a factor of approximately 3.4. At $Ra = 10^6$ the radial velocity now exhibits a strong dependence on Reynolds number, with peak boundary layer velocity decreasing by more than 10% from $Re = 10$ to $Re = 100$, and then to negligibly small values for $Re = 320$ and beyond. From $Re = 10$ to 100, $u_{\theta,rel}$ initially exhibits the expected increase with Reynolds number, but at higher Reynolds numbers the rapid vanishing of u_r carries $u_{\theta,rel}$ down to very small values. While it cannot be seen directly from Fig. 8(b), by $Re = 1000$ at $Ra = 10^6$, $u_{\theta,rel}$ exceeds u_r by greater than 10%: the boundary layer is dominated by azimuthal rather than radial transport. The relative temperature profile further exemplifies this observation, with $Re = 10$ and 100 exhibiting a local temperature

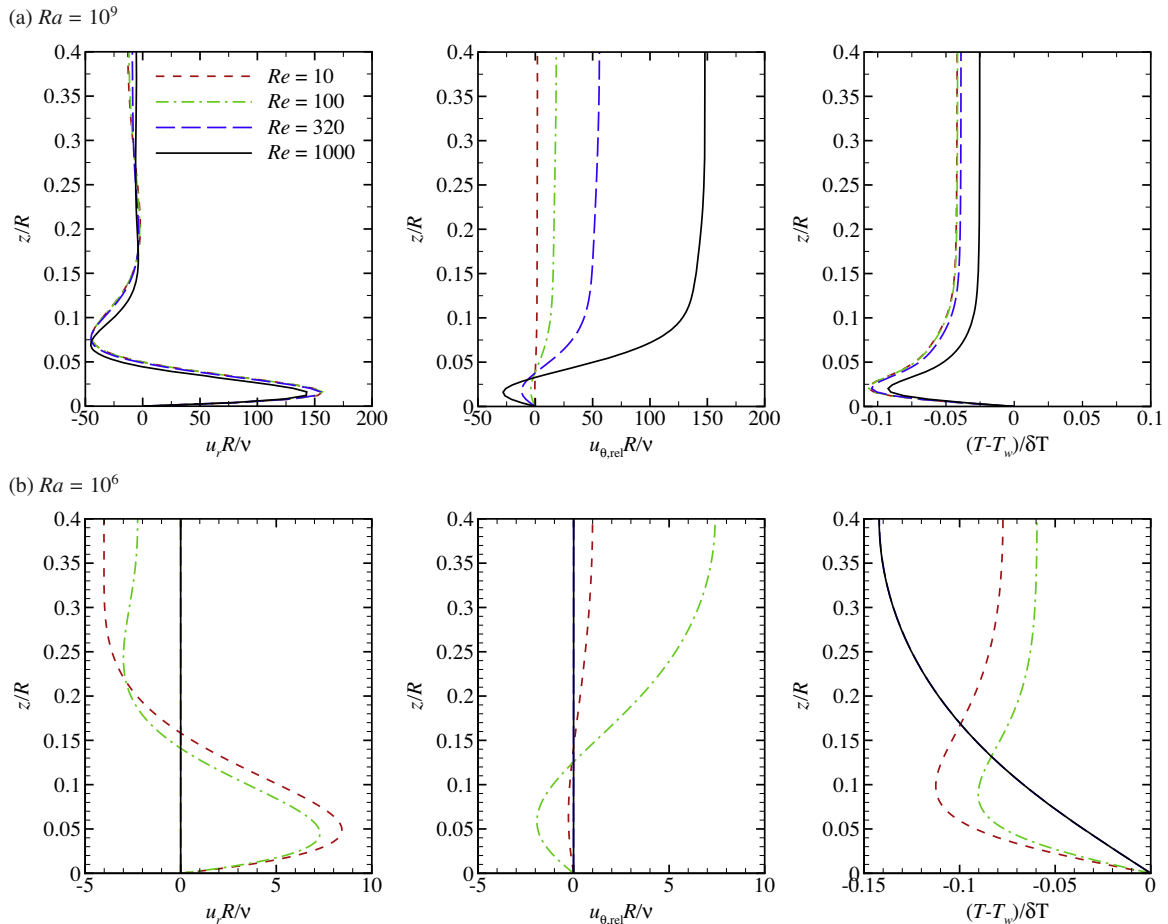


Fig. 8. Plot showing z variation of u_r , $u_{\theta,rel}$ and temperature relative to local wall temperature at $r/R = 0.9$. Rayleigh numbers (a) $Ra = 10^9$ and (b) 10^6 are shown. In (a), $Re = 10$ to 1000 correspond to $Q = 0.005$, 0.050 , 0.161 , and 0.502 , respectively. In (b), the corresponding values are $Q = 0.080$, 0.796 , 2.55 and 7.97 , respectively.

minimum in the boundary layer consistent with a convective boundary layer, whereas the profiles at $Re = 320$ and beyond are coincident and display a monotonic decrease throughout the domain. This is consistent with a conductive process, and demonstrates that the increase in Reynolds number (beyond some value) serves to shut down radial horizontal convective flow in the rotating system. At this Rayleigh number, the $Re = 10$ and 100 cases correspond to $Q < 1$, and lie within the convection-dominated regime III as per Fig. 5. Conversely, $Re = 320$ and 1000 have $Q > 1$ and hence lie within regime II. The significant change in the velocity profiles seen here demonstrates the emerging importance of rotation as the threshold $Q \approx 1$ is exceeded.

The validity of Eq. (26) is further evidenced by considering the ratio of azimuthal to radial wall shear stress on the forcing boundary. Under the scaling analysis deployed earlier, this ratio of wall shear stresses will have the same scaling as the ratio of $u_{\theta,rel}$ to u_r in the boundary layer (as the vertical length differentials cancel). It would then be expected from Eq. (26) that the wall shear stress ratio would vary linearly with Re and would vary with $Ra^{-1/5}$. Fig. 9 plots the absolute values of the ratio of wall shear stresses on a logarithmic scale as a function of r/R . The sharp downward spikes in each data set occurs as the azimuthal shear stress changes sign as the relative azimuthal velocity in the boundary layer switches from advancing to lagging the tank rotation through the Coriolis effect (Ref. Fig. 6). The area of interest is near the hot outer wall (towards $r/R = 1$). In this region, an excellent agreement with the Reynolds-number-scaling predicted by Eq. (26) is observed. In Fig. 9(a), an almost perfect decade increase in the ratio with a decade increase

in Reynolds number, following the expected Re^1 scaling. In Fig. 9(b), a decade increase in Rayleigh number produces a decrease in the logarithm of the wall shear stress ratio of between 0.3 and 0.5 , which is a little higher than the expected interval of 0.2 .

To gain further insight into how the boundary layer thickness is affected by Rayleigh number, the velocity and thermal boundary layer thicknesses measured at $r/R = 0.5$ are examined. Thicknesses were calculated from the radial velocity and temperature profiles, and the results are plotted against Rayleigh number in Fig. 10. The velocity boundary layer thickness is taken as the distance from the base to the point of maximum velocity in the boundary layer, and the thermal boundary layer thickness is taken to be the distance between the base and the point in the profile where the temperature first departs 5% from the temperature at the top wall. It can be noted that at low Rayleigh number, the velocity boundary layer thicknesses δ_U/R are Reynolds number dependent. As Ra is further increased beyond $\approx 10^9$ (the convective dominated regime), the velocity boundary layer thickness curves becomes independent of Reynolds number. However, the thermal boundary layer thicknesses δ_T/R are found to be Reynolds number independent in the diffusion regime ($Ra \lesssim 10^5$), but remain more strongly independent of Reynolds number in much of the convective regime. Considering an increasing Rayleigh number, at zero Reynolds number both δ_U/R and δ_T/R curves collapse to single trends with gradients of approximately $-1/5$, which agrees well with the prediction of Eq. (22).

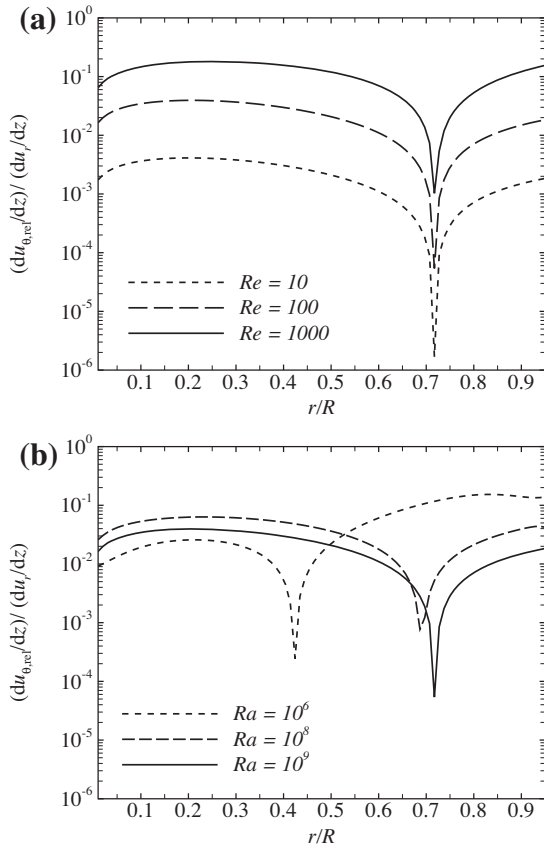


Fig. 9. Plots of the ratio of azimuthal to radial wall shear stress against r/R . (a) $Ra = 10^9$ is shown for Reynolds numbers as indicated. (b) $Re = 100$ for various Rayleigh numbers as indicated. In order of increasing Reynolds number in (a), the cases correspond to $Q = 0.005, 0.050$ and 0.502 , respectively. With increasing Rayleigh number in (b), the cases correspond to $Q = 0.796, 0.126$ and 0.050 , respectively.

5.4. Flow structure in the diffusion and convection regimes

We now turn our attention to the flow fields within the enclosure. Figs. 11 and 12 plot the temperature and relative azimuthal velocity for $Re = 3.2$ and 1000 , respectively, at different Rayleigh numbers. Despite the substantially different Reynolds numbers, the Rayleigh number range is sufficient to span regime I through to regime III in both cases. Across both figures, regime I presents temperature fields exhibiting a smooth and gradual variation throughout the enclosure. At the base, the isotherms are nearly vertical, and there is no evidence of any convective boundary layer formation. The regime II cases each exhibit a thin region above the base where the isotherms slant away from the axis, whereas further from the base the isotherms slant back towards the axis. This behaviour is consistent with the development of a weak horizontal convection boundary layer, but rotation effects have substantially altered the overall topology of the temperature field. Regime III presents a thin boundary layer on the base (where temperature changes rapidly in the vertical direction), and a large region of nearly constant-temperature fluid (Ref. Fig. 8(b)) extending from the edge of the boundary layer to the free surface. This isothermal region is absent in regime II.

The effect of higher Reynolds number in delaying the onset of regimes II and III is apparent. It is interesting to compare these contour plots to both the corresponding Nusselt number data in Figs. 2 and 3, and the regime map in Fig. 5.

In Ref. [14], horizontal convection was computed within a rectangular enclosure at high rates of rotation. Simulations in that

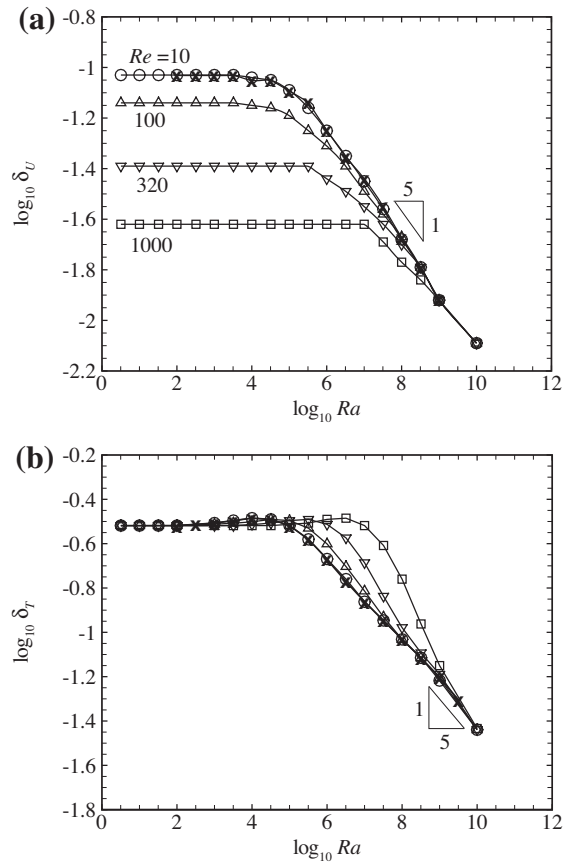


Fig. 10. A plot of the logarithm of (a) velocity boundary layer thickness and (b) thermal boundary layer thickness against $\log_{10} Ra$ for different Reynolds number as indicated. Symbol (\times) represents $Re = 0$.

study where out-of-plane flow variations were suppressed (akin to the axisymmetric solutions reported in the present paper) showed that the flows at high rotation rates lacked a boundary layer at the thermal forcing boundary (the top boundary in that study), and exhibited weaker overturning circulation. That finding is consistent with the computed flow fields presented here, where higher rotation rates (higher Re) suppresses the convective regime for a given Rayleigh number, and rotational effects are seen to weaken and substantially modify the thermal convection in regime II (where $Q > 1$) compared to regime III (where $Q < 1$).

Another notable feature from Figs. 11 and 12 pertains to the relative azimuthal velocity field. In the diffusion-dominated regime, a region of high $u_{0,rel}$ is located approximately half the distance to the side wall, gradually diminishing to zero at the axis, base and side-wall. In regimes I and II, this positive- $u_{0,rel}$ region is accompanied by a smaller negative- $u_{0,rel}$ region spread across the entire base. As the convection-dominated regime III is entered, the $u_{0,rel}$ field exhibits a marked change in character. The zone of higher $u_{0,rel}$ expands downward, filling much of the enclosure depth with fluid swirling faster than the tank rotation speed. Coupled with this, demonstrated most strongly at $Ra = 10^9$ in Fig. 12, there is a strong depth-independence outside of the forcing boundary layer. There is an ongoing interest in the study of barotropic instability in depth-independent rotating shear layers [10,11]; the ability of this system to produce nearly depth-independent flows at higher Reynolds numbers and Rayleigh numbers suggest an unexpected possible new application of this system. Additionally, in regime III the zone of negative- $u_{0,rel}$ ceases to span the entire base and instead becomes confined to the outer bottom corner of the enclosure.

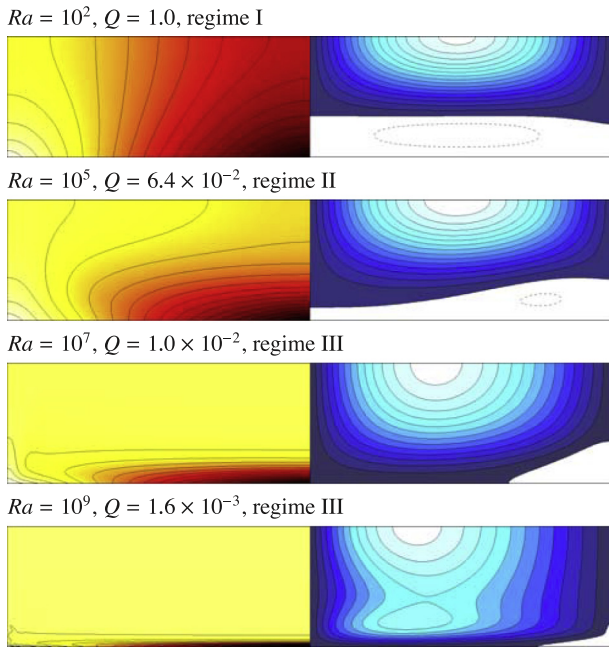


Fig. 11. Contour plots of temperature (left) and azimuthal velocity relative to the tank rotation ($u_{\theta,rel}$, right) at $Re = 3.2$ and Rayleigh numbers, Q -values and regime numbers (refer to Fig. 5) as indicated, plotted on a meridional cross-section through the centre of the tank (so that the frames meet at the symmetry axis). Dark to light temperature contours show temperatures ranging from $0 \leq T \leq \delta T$, relative to the bottom wall temperature at $r = 0$, at increments of $0.05\delta T$. Dark to light contours of $u_{\theta,rel}$ show zero to maximum values of the relative azimuthal velocity, respectively. Negative values are shaded white with dashed contour lines. The minimum and maximum levels of $u_{\theta,rel}$ for $Ra = 10^2, 10^5, 10^7$ and 10^9 , respectively, are -2×10^{-5} to $3.2 \times 10^{-4}, -1 \times 10^{-2}$ to $0.14, 0$ to 0.65 and 0 to 1.1 .

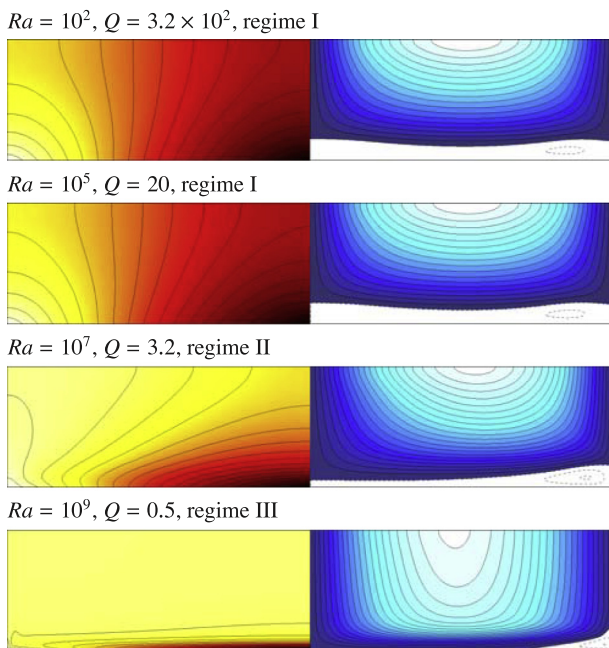


Fig. 12. As per Fig. 11, except here $Re = 1000$. Here the minimum and maximum levels of $u_{\theta,rel}$ for $Ra = 10^2, 10^5, 10^7$ and 10^9 , respectively, are -1×10^{-7} to $1.7 \times 10^{-6}, -1 \times 10^{-4}$ to $1.7 \times 10^{-3}, -1 \times 10^{-2}$ to 1.5×10^{-2} and -5×10^{-2} to 0.475 .

6. Conclusion

We have investigated the effect of rotation on the heat transport in horizontal convection in a cylindrical system, with horizon-

tal convection forcing imposed radially. Numerical simulations and a scaling analysis have considered the axisymmetric flow in a free surface cylindrical enclosure with constant rotation, with the radial temperature profile at the base driving convection in the $z-r$ plane. A scaling analysis of the convective forcing boundary layer yields predictions for variation in boundary layer thickness, Nusselt number, and velocity components with Reynolds number, Rayleigh number and Prandtl number. Simulations at Reynolds number up to 3200 and Rayleigh numbers up to 3.2×10^{11} demonstrate that heat transfer in rotating horizontal convection is significantly affected by rotation. Following Hignett et al. and Barkan et al., it is helpful to characterise the flow using Q , a parameter representing the ratio of the scales of the thermal boundary layer to the Ekman layer.

Three regimes are identified when characterising the flow as a function of Reynolds number (characterising rotation rate) and Rayleigh number (characterising thermal forcing). At low Rayleigh numbers, the flow is dominated by diffusion and the Nusselt number is constant and independent of Reynolds number (regime I). At higher Rayleigh numbers, convection effects become significant and the Nusselt number begins increasing with Rayleigh number. Where $Q < 1$, rotation is not significant and the flow adheres to the same scaling as found for planar horizontal convection without rotation (regime III), despite the forcing acting radially in a cylindrical enclosure, rather than linearly in a rectangular enclosure. This scaling behaviour is supported by the scaling analysis developed in Section 3. When rotation effects are significant (regime II, $Q > 1$), moderate rotation rates produce behaviour adhering to the scalings developed from Robinson and Stommel and Park and Whitehead. At higher rotation rates, the scaling proposed by Stern is found to describe the behaviour very well. The applicability of these scalings is found to extend to describing the critical Reynolds number for the onset of convective flow (the threshold between regimes I and II) as well as describing the Nusselt number scaling within regime II. This confirms that at higher rotation rates, Stern's argument holds: namely that buoyancy flux should dominate throughout the thermal boundary layer while dissipation is confined to the Ekman layer, rather than there being a balance between advection and vertical diffusion in the buoyancy equation.

A regime map for the axisymmetric flow as functions of Rayleigh number and Reynolds number is constructed, which shows an expanding range of Rayleigh numbers over which rotation is significant with increasing Reynolds number.

Independent of Reynolds number (up to $Re = 3200$), unsteady flow at thermal equilibrium is found to occur between $Ra = 3.2 \times 10^9$ (where the flow was consistently steady-state) and $Ra = 10^{10}$ (where the flow was consistently time-periodic). The radial nature of the thermal forcing in the present system serves to delay the onset of unsteady flow by approximately an order of magnitude in Rayleigh number when compared to planar horizontal convection (where our high-resolution simulations find unsteady flow at and beyond $Ra = O(10^9)$). For both planar and radial horizontal convection forcing, the flow first transitions from steady to time-periodic flow, then approximately an order of magnitude higher in Rayleigh number, from periodic to irregular unsteady flow.

Contour plots of temperature and relative azimuthal velocity at multiple Rayleigh and Reynolds numbers reveal that regimes I, II and III produce distinctively different flows.

Conflict of interest

None declared.

Acknowledgments

This project is supported by ARC Discovery Grant DP120100153. Numerical simulations were made possible thanks to high-performance computing time allocations from the National Computational Infrastructure (NCI) Merit Allocation Scheme, the Victorian Life Sciences Computation Initiative (VLSCI) Resource Allocation Scheme, and the Monash SunGRID. We are grateful for the insights of the two anonymous reviewers whose suggestions significantly improved this paper.

References

- [1] Y.-G. Park, J. Whitehead, Rotating convection driven by differential bottom heating*, *J. Phys. Oceanogr.* 29 (1999) 1208–1220.
- [2] M.E. Stern, *Ocean Circulation Physics*, vol. 246, Academic Press, New York, 1975.
- [3] G.O. Hughes, R.W. Griffiths, Horizontal convection, *Ann. Rev. Fluid Mech.* 40 (2008) 185–208.
- [4] J.-Q. Zhong, R.J.A.M. Stevens, H.J.H.C.R. Verzicco, D. Lohse, G. Ahlers, Prandtl-, Rayleigh-, and Rossby-number dependence of heat transport in turbulent rotating Rayleigh–Bénard convection, *Phys. Rev. Lett.* 102 (2009) 44502.
- [5] E.M. King, S. Stellmach, J.M. Aurnou, Heat transfer by rapidly rotating Rayleigh–Bénard convection, *J. Fluid Mech.* 691 (2012) 568–582.
- [6] J. Marshall, F. Schott, Open-ocean convection: observations, theory, and models, *Rev. Geophys.* 691 (1999) 1–64.
- [7] G.A. Glatzmaier, R.S. Coe, L. Hongre, P.H. Roberts, The role of the Earth's mantle in controlling the frequency of geomagnetic reversals, *Nature* 401 (1999) 885–890.
- [8] G.A. Glatzmaier, R.S. Coe, L. Hongre, P.H. Roberts, Convection driven zonal flows and vortices in the major planets, *Chaos* 4 (1994) 123–134.
- [9] M.S. Miesch, The coupling of solar convection and rotation, *Sol. Phys.* 192 (2000) 59–89.
- [10] A.C.B. Aguiar, P.L. Read, R.D. Wordsworth, T. Salter, Y.H. Yamazaki, A laboratory model of Saturn's north polar hexagon, *Icarus* 206 (2010) 755–763.
- [11] T. Vo, L. Montabone, G.J. Sheard, Linear stability analysis of a shear layer induced by differential coaxial rotation within a cylindrical enclosure, *J. Fluid Mech.* 738 (2014) 299–334.
- [12] H.T. Rossby, On thermal convection driven by non-uniform heating from below: an experimental study, *Deep Sea Research and Oceanographic Abstracts*, vol. 12, Elsevier, 1965, pp. 9–16.
- [13] P. Hignett, A. Ibbetson, P.D. Killworth, On rotating thermal convection driven by non-uniform heating from below, *J. Fluid Mech.* 109 (1981) 161–187.
- [14] R. Barkan, K.B. Winters, S.G. Llewellyn Smith, Rotating horizontal convection, *J. Fluid Mech.* 723 (2013) 556–586.
- [15] R. Smith, Longitudinal dispersion of a buoyant contaminant in a shallow channel, *J. Fluid Mech.* 78 (1976) 677–688.
- [16] J. Whitehead, Laboratory models of circulation in shallow seas, *Philos. Trans. Roy. Soc. Lond. Ser. A, Math. Phys. Sci.* 302 (1981) 583–595.
- [17] A. Robinson, H. Stommel, The oceanic thermocline and the associated thermohaline circulation I, *Tellus* 11 (1959) 295–308.
- [18] T. Rossby, Numerical experiments with a fluid heated non-uniformly from below, *Tellus A* 50 (1998) 242–257.
- [19] G.J. Sheard, M.P. King, Horizontal convection: effect of aspect ratio on Rayleigh number scaling and stability, *Appl. Math. Model.* 35 (2011) 1647–1655.
- [20] J.C. Mullarney, R.W. Griffiths, G.O. Hughes, Convection driven by differential heating at a horizontal boundary, *J. Fluid Mech.* 516 (2004) 181–209.
- [21] G.E. Karniadakis, M. Israeli, S.A. Orszag, High-order splitting methods for the incompressible Navier–Stokes equations, *J. Comput. Phys.* 97 (1991) 414–443.
- [22] G.J. Sheard, K. Ryan, Pressure-driven flow past spheres moving in a circular tube, *J. Fluid Mech.* 592 (2007) 233–262.
- [23] G.J. Sheard, Flow dynamics and wall shear-stress variation in a fusiform aneurysm, *J. Eng. Math.* 592 (2007) 233–262.
- [24] W.K. Hussam, M.C. Thompson, G.J. Sheard, Dynamics and heat transfer in a quasi-two-dimensional MHD flow past a circular cylinder in a duct at high Hartmann number, *Int. J. Heat Mass Trans.* 54 (2011) 1091–1100.
- [25] W.K. Hussam, M.C. Thompson, G.J. Sheard, Enhancing heat transfer in a high Hartmann number magnetohydrodynamic channel flow via oscillation of a cylindrical obstacle, *Phys. Fluids* 24 (2012) 113601.
- [26] W.K. Hussam, G.J. Sheard, Heat transfer in a high Hartmann number MHD duct flow with a circular cylinder placed near the heated side-wall, *Int. J. Heat Mass Trans.* 67 (2013) 944–954.
- [27] G.J. Sheard, M.P. King, The influence of height ratio on the stability of horizontal convection, in: P.J.W. M.P. Schwarz (Ed.), *Proceedings of the Seventh International Conference on Computational Fluid Dynamics in the Minerals & Process Industries*, CSIRO Australia, Rydges Hotel, Melbourne, Australia, 2009, pp. 096SHE.
- [28] F. Paparella, W.R. Young, Horizontal convection is non-turbulent, *J. Fluid Mech.* 466 (2002) 205–214.
- [29] J. Siggers, R. Kerswell, N. Balmforth, Bounds on horizontal convection, *J. Fluid Mech.* 517 (2004) 55–70.
- [30] K.Y. Wong, M.P. King, G.J. Sheard, Horizontal convection in an enclosure with fixed and moving walls, in: G.D. Mallinson, J.E. Cater (Eds.), *Proceedings of the 17th Australasian Fluid Mechanics Conference*, The University of Auckland, The University of Auckland, Auckland, New Zealand, 2010, pp. 351.
- [31] A. Scotti, B. White, Is horizontal convection really non-turbulent, *Geophys. Res. Lett.* 38 (2011).
- [32] M. Ilıcak, G.K. Vallis, Simulations and scaling of horizontal convection, *Tellus A* 64 (2012).
- [33] B. Gayen, R.W. Griffiths, G.O. Hughes, J.A. Saenz, Energetics of horizontal convection, *J. Fluid Mech.* 716 (2013) R10.
- [34] S. Chandrasekhar, The instability of a layer of fluid heated below and subject to coriolis forces, *Proc. Roy. Soc. Lond. Ser. A, Math. Phys. Sci.* 217 (1953) 306–327.
- [35] S. Chandrasekhar, D.D. Elbert, The instability of a layer of fluid heated below and subject to Coriolis forces. II, *Proc. Roy. Soc. Lond. Ser. A, Math. Phys. Sci.* 231 (1955) 198–210.